Chinese Chemical Letters 31 (2020) 2784–2788

Contents lists available at ScienceDirect

Chinese Chemical Letters

journal homepage: www.elsevier.com/locate/cclet

Communication

Efficient singlet oxygen generation by excitonic energy transfer on ultrathin g-C_3N_4 for selective photocatalytic oxidation of methyl-phenyl-sulfide with O_2

Fan Yang[a], Xiaoyu Chu[a,b], Jianhui Sun[a,*], Yuhang Zhang[a], Zhijun Li[a], Haiyue Liu[a], Linlu Bai[a,b], Yang Qu[a,*], Liqiang Jing[a,*]

[a] Department Key Laboratory of Functional Inorganic Materials Chemistry (Heilongjiang University), Ministry of Education, School of Chemistry and Materials Science, International Joint Research Center and Lab for Catalytic Technology, Harbin 150080, China
[b] School of Chemical and Environmental Engineering, Harbin University of Science and Technology, Harbin 150080, China

ARTICLE INFO

Article history:
Received 12 June 2020
Received in revised form 28 June 2020
Accepted 7 July 2020
Available online 17 July 2020

Keywords:
g-C_3N_4 nanosheet
Singlet oxygen generation
Excitonic energy transfer
Photocatalysis
Organic selective oxidation

ABSTRACT

Efficient generation of singlet oxygen ($^1O_2$) by an excitonic energy transfer process is highly desired on a semiconductor photocatalyst for selective oxidation of methyl phenyl sulfide (MPS). Herein, it is demonstrated that a large amount of $^1O_2$ is produced on pristine graphitic carbon nitride (CN) nanosheet compared with bismuth oxybromide (BiOBr) and commercial P25 titanium dioxide (TiO_2). This leads to a certain photoactivity of CN for MPS oxidation. The observed ~77% selectivity for CN depends on the competitive results of excitonic energy transfer for $^1O_2$ formation and charge carrier separation for superoxide radical ($O_2^{\bullet-}$) production, which are based on the phosphorescence spectra and electron paramagnetic resonance signals, respectively. Moreover, ultrathin CN nanosheets are synthesized by thermal treatment with the cyanuric acid-melamine hydrogen bonded aggregates as precursors. It is confirmed that the amount of produced $^1O_2$ could be increased by decreasing the thickness of resultant CN nanosheets. The optimized ultrathin CN nanosheet (~4 nm) exhibits excellent photoactivity with high selectivity (~99%). It is suggested that the excitonic energy transfer for $^1O_2$ formation is close related to the intrinsic exciton binding energy and the two-dimensional quantum confinement effect. This work establishes a basic mechanistic understanding on the excitonic processes in CN, and develops a feasible route to design CN-based photocatalysts for efficient $^1O_2$ generation.

For decades, selective oxidation plays an important role in environmental and green chemistry, which can reduce pollutant production and resource consumption in the chemical reactions [1–4]. As one of the most important oxidization agents for selective conversion, singlet oxygen ($^1O_2$) is the key for selective oxidation [5,6]. However, it is usually difficult for efficient $^1O_2$ generation, mainly dependent on the energy transfer process between a photocatalyst and ground state oxygen ($^3O_2$) [7,8], to be realized owing to the current lack of mechanistic understanding on the correlated energy transfer processes and the impertinent use of the photocatalysts.

Various photocatalysts, including semiconductors, noble metal nanoparticles and organic dye-containing materials, have been exploited for energy conversion in the last few decades [9–11]. Among these photocatalysts, semiconductors have captured widespread research interest because of their design flexibility and high stability in practical applications. In particular, titanium dioxide (TiO_2) as a rather popular one has attracted great attention for a long time and is considered as one of the most promising photocatalysts for commercial use due to its outstanding optical-electrical properties, photoactivity and eco-friendliness [12]. As for TiO_2, it is much preferential to produce superoxide radical ($O_2^{\bullet-}$) and hydroxyl radical ($^{\bullet}OH$) by photoinduced charge separation rather than $^1O_2$ by excitonic energy transfer, meaning that it is not feasible for selective oxidation with TiO_2 [13]. Noticeably, bismuth oxybromide (BiOBr) and pristine graphitic carbon nitride (CN) with their exotic layered structure in morphology always exhibit remarkable performance in photocatalytic energy conversion in recent years. It is worth noting that both BiOBr and pristine CN could be adopted as the efficient photocatalysts for selective oxidation reactions with the involvement of $^1O_2$ [7,8]. It is reported

* Corresponding authors.
E-mail addresses: sunjh298@hlju.edu.cn (J. Sun), quyang@hlju.edu.cn (Y. Qu), jinglq@hlju.edu.cn (L. Jing).

https://doi.org/10.1016/j.cclet.2020.07.033
1001-8417/

that the low-dimensional layered structure usually has excellent photocatalytic performance in $^1O_2$ generation [14]. As well known, $^1O_2$ can be produced *via* the essential energy transfer from an exciton on a photocatalyst by reacting with $^3O_2$ [5], indicating that the excitons in photocatalysts are essential for the production of $^1O_2$. In general, the large intrinsic exciton binding energy is favorable to form more excitons on a photocatalyst. Noticeably, pristine CN usually exhibits much more attractive prospect for the design of advanced photocatalysts for $^1O_2$ generation [8,15,16], probably due to its intrinsic large exciton binding energy of ~328 meV [17]. As compared to bulk counterparts, low-dimensional layered structures tend to appear the predominant inplanar electronic transport process [18], leading to significant electron-hole interactions and large exciton binding energies [19]. Obviously, it is meaningful to carry out a comparative investigation on several widely-employed photocatalysts for revealing the main factors to influence the excitonic energy transfer and then the $^1O_2$ generation. Unfortunately, it has seldom been reported up to date.

Although CN as a potential photocatalyst could be used for selective oxidation reactions with the involvement of $^1O_2$, where the $^3O_2$ molecular activation behavior in such kind of conjugated polymers could be regulated *via* excitonic strategy, the regulation effect of two-dimensional (2D) layered structure on excitons is seldom involved, and the basic mechanistic understanding on the excitonic processes in CN is unclear. The Coulomb interactions between electrons and holes in a semiconductor will be improved when its particle size becomes very small owing to the quantum confinement effect [20,21], leading to the formation of more excitons. Therefore, it is much meaningful to further investigate the effects of 2D confined layered structures on the involved excitonic processes and then the resulting efficient $^1O_2$ generation. This intriguing issue encourages us to prepare ultrathin CN nanosheets with the strong excitonic effects on the photocatalytic processes.

Herein, by taking the typical low-dimensional semiconductors like pristine CN and BiOBr, and TiO_2 as examples, we have systematically compared the photoexcitation processes involved in these materials by combining surface photocurrent (SPC) test [22,23], phosphorescence (PH) spectroscopy [24–26] and electron paramagnetic resonance (EPR) spectroscopy [27,28], highlighting the influence of excitonic aspects on the photocatalytic performance for selective oxidation. The $^1O_2$ generation with a maximum yield is observed in the pristine CN due to its strongest exciton effect among the three semiconductors, leading to a superior selectivity of ~77% in oxidation of methyl phenyl sulfide (MPS). Moreover, the regulation effect of the CN layered structure on excitons has been evaluated according to the 2D quantum confinement effect, and it is confirmed that the amount of produced $^1O_2$ could be greatly increased when the thickness of resultant CN nanosheets is reduced to ~4 nm, displaying an excellent photoactivity with high selectivity (99%). The significant performance improvement sets a valuable strategy through exciton regulation for designing new class of CN photocatalyst materials with highly effective $^1O_2$ generation in selective oxidation reactions.

As shown in Fig. S1a (Supporting information), the X-ray powder diffraction (XRD) pattern of the pristine CN shows two typical diffraction peaks of (100) and (002), which are in accordance with the previous report [6,29]. Meanwhile, the band gap of the pristine CN is determined to be 2.67 eV according to the ultraviolet-visible (UV–vis) spectra (Fig. S1b in Supporting information). One can see from the transmission electron microscopy (TEM) image (Fig. 1a) that the pristine CN displays the plate-like morphology with lateral dimensions of more than 10 micrometers, and there is no visible lattice fringe in its high-resolution transmission electron microscopy (HRTEM) (Fig. 1b). For

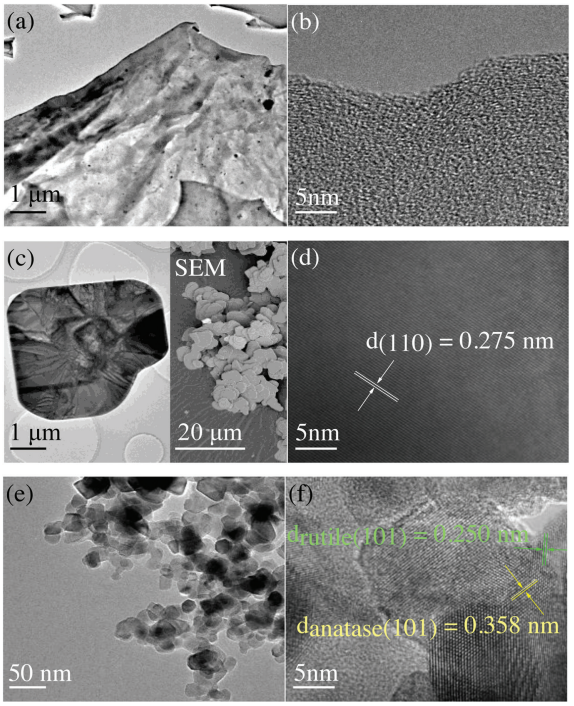

Fig. 1. TEM (a) and HRTEM (b) images of pristine CN nanosheets, TEM (c) and HRTEM (d) images of BiOBr, and TEM (e) and HRTEM (f) images of P25 TiO_2. The inset in figure c is a low-magnification SEM image for BiOBr.

BiOBr, it is confirmed by the specific XRD pattern (JCPDS No. 73-2061), suggesting its high purity (Fig. S1a). The relative intensity of the (001) peak is significantly higher than those of other crystal facets, indicating its plate-like morphology. Such plate-like morphology is also confirmed from the TEM image and scanning electron microscopy (SEM) image of BiOBr in the Fig. 1c. Besides, the HRTEM image of BiOBr in Fig. 1d shows a lattice fringe of about 0.275 nm that is closed to the lattice fringe of (110) facet of the BiOBr. The band gap of the BiOBr is determined to be 2.80 eV from the UV–vis spectra (Fig. S1b).

As shown in Fig. 1e, the TEM image of the P25 TiO_2 displays the morphology of spherical particle with an average diameter of ~25 nm, which is markedly different from the observed morphology of the pristine CN and BiOBr with the typical layered structures. It is confirmed from the XRD pattern of P25 TiO_2 in Fig. S1a that there is a mixed-phase composition with the diffraction peaks respectively assigned to the typical anatase structure (JCPDS No. 21-1272) and rutile structure (JCPDS No. 21-1276) (Fig. S1a), which is also proved by the HRTEM image with the characteristic lattice fringes of anatase structure ($d_{(101)}$, about 0.358 nm) and rutile structure ($d_{(101)}$, about 0.250 nm) in Fig. 1f. The band gap of the P25 TiO_2 is determined to be ~3.10 eV according to the UV–vis spectra (Fig. S1b).

Considering that the specific surface area is critical for the performance of photocatalyst, the Brunauer-Emmett-Teller (BET) measurements were carried out on the three resulting photocatalysts. Concretely, the specific surface areas of the pristine CN, BiOBr and P25 TiO_2 are determined to be 7.8, 2.8 and 51.7 m^2/g, respectively (Table S1 in Supporting information). It is obvious that the surface area of P25 TiO_2 is much larger than those of the pristine CN and BiOBr.

To identify the exciton effects and analyze the competitive relationship between excitons and free carriers on the three resulting photocatalysts [30,31], the SPC and PH tests were performed. As seen in Fig. S2a (Supporting information), the steady-state SPC spectra measured in nitrogen (N_2) at room

temperature exhibit the initial positions at ~410 nm for P25 TiO_2 and ~440 nm for BiOBr, assigned to their intrinsic absorption band edges with the energies which are in accordance with the band gaps of ~3.10 eV and ~2.80 eV, respectively. It also can be seen that the SPC signal peak of P25 TiO_2 is about 7.5-time higher than that of BiOBr, which is inconsistent with their similar absorbance densities as shown in Fig. S1b. As known, excitons and free charges are produced concomitantly in photocatalysts under light irradiation, and the SPC signal only comes from the free carriers *via* the efficient charge separation other than the excitons. Thus, it is deduced that P25 TiO_2 exhibits a high photogenerated charge separation, while BiOBr does a relatively obvious exciton characteristic. For P25 TiO_2, its excitons are easily dissociated to form free charge carriers since the exciton binding energy of P25 TiO_2 is as low as about ~4 meV [32], which is far below the value of thermal energy (~26 meV) [33] at room temperature. Differently, the excitons in BiOBr have been identified previously with an intrinsic exciton binding energy of ~280 meV [14]. That is to say, the large intrinsic exciton binding energy of BiOBr is responsible for the weak SPC intensity, which is ascribed to the strong Coulomb interaction between electrons and holes in the BiOBr due to its 2D confined layered structure.

Similar to the BiOBr with the 2D confined layered structure, pristine CN as an organic semiconductor is nearly no SPC signal because of its largest intrinsic exciton binding energy of ~328 meV [17] and its much thinness. Therefore, it seems that the photocatalysts with 2D confined layered structures could intrinsically enhance the Coulomb interaction between electrons and holes and thus generally possess more excitons. Moreover, the excitons can translate into triplet excitons through the intersystem crossing (ISC) process and the triplet excitons normally return to the ground singlet state, resulting in the PH emission. This allows us to perform the PH measurement to directly evaluate the density of triplet excitons and to understand the feature of involved exciton effects in photocatalysts. As shown in Fig. 2a, the PH spectra of three photocatalysts were recorded in N_2 at room temperature. There is no detective PH emission in P25 TiO_2 and BiOBr. It is easily understood for no PH signal in TiO_2 since it has high charge separation, while it is attributed to the too weak PH signal for BiOBr. As expected, the pristine CN exhibits a strong PH emission with an emission peak centering at about 500 nm wavelength, indicating the large density of triplet excitons. Interestingly, PH quenching effects in the pristine CN by the $^3O_2$ molecules were investigated to understand the excitonic energy transfer process [34,35]. As shown in Fig. 2b, the PH emission of the pristine CN is greatly quenched by the $^3O_2$ molecules, which is ascribed to the energy transfer process from triplet excitons to $^3O_2$ to form $^1O_2$. The energy transfer process is further confirmed by the time-resolved PH spectra in Fig. S2b (Supporting information), by which it is confirmed that the average PH lifetime is shortened from 2.54 ms in N_2 to 2.30 ms in $^3O_2$, suggesting that the $^1O_2$ generation has the close correlation to the PH quenching process in $^3O_2$.

In order to confirm the $^1O_2$ generation, designed EPR measurements were performed. The 2,2,6,6-Tetramethyl-4-piperidinol was employed as the trapping agents for $^1O_2$ in ethanol solvent and then the corresponding EPR spectra display a 1:1:1 triplet signal for $^1O_2$ [27,28]. As illustrated in Fig. 2c, a much strong 1:1:1 triplet signal with a g-factor value of 2.005 arises in the presence of pristine CN compared to that in BiOBr under light irradiation for 30 s without any optical filter, whereas it is nearly no signal for P25 TiO_2, indicating that the larger amounts of $^1O_2$ generation on pristine CN than that on BiOBr and there is almost no $^1O_2$ generation in P25 TiO_2. The $^1O_2$ is deemed as a green and effective oxidant for selective conversion of sulfide to sulfoxide and thus the photocatalytic activities of three photocatalysts were further evaluated by selective sulfoxidation reaction for methyl phenyl sulfide (MPS).

As shown in Fig. 2d, the conversion rate for P25 TiO_2 is only ~1%, suggesting that MPS is hard to be converted on P25 TiO_2. Differently, pristine CN and BiOBr exhibit the high conversion rates, and the former (~16%) is higher than the latter (~10%). In addition, the selectivity of the reactions was investigated. Expectedly, P25 TiO_2 shows a low selectivity (~2%), while the pristine CN and BiOBr show much high selectivities of ~77% and ~60%, respectively. By comparison, it is clearly demonstrated that the conversion rate and selectivity are close related to the amount of generated $^1O_2$, especially for the selectivity. Besides, $O_2^{\bullet-}$ as the product of photogenerated charge separation would have certain effects on the final the conversion rate and selectivity [36–38]. To further clarify this, designed EPR measurements by employing the 5,5-dimethyl-1-pyrrolinen-oxide (DMPO) as the trapping agents for $O_2^{\bullet-}$ in the solvent were performed. As illustrated in Fig. S2c (Supporting information), the corresponding EPR spectra with a 1:1:1:1 quartet signal indicate the amount of generated $O_2^{\bullet-}$ on pristine CN is a little small compared to that on BiOBr. However, P25 TiO_2 displays a rather small amount of generated $O_2^{\bullet-}$ in acetonitrile system, which is different from the widely-accepted high charge separation in water as shown in Fig. S2d (Supporting information). Thus, it is deduced that the conversion rate mainly depends the amount sum of generated $^1O_2$ *via* the excitonic energy transfer and $O_2^{\bullet-}$ *via* the charge separation process, while the ratio of $^1O_2$ amount to the sum determine the final selectivity.

In order to investigate the regulation effect of 2D layered structure on the excitonic energy transfer and then the formed $^1O_2$, different thicknesses of ultrathin $CN_{1:X}$ nanosheets are designed to prepare. The molecular cooperative assembly method was developed to alter thickness of the CN by changing the amount of cyanuric acid used in the formed cyanuric acid-melamine hydrogen bonded aggregates [29]. As shown in Fig. 3a, the crystal structures of the resulting different thicknesses of ultrathin $CN_{1:X}$ nanosheets were characterized by XRD patterns, where all the ultrathin $CN_{1:X}$ nanosheets show typically diffraction peaks of (100) and (002), in accordance with the reported crystal structure of CN nanosheets [6,29]. Compared with the pristine CN, the XRD

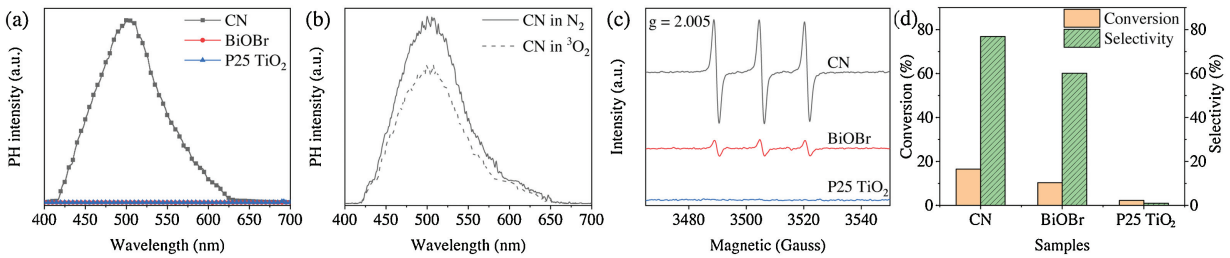

Fig. 2. Phosphorescence (PH) spectra (a) of pristine CN, BiOBr and P25 TiO_2 (1 ms of delay time, excitation wavelength at 365 nm), PH spectra (b) of pristine CN in N_2 and $^3O_2$, EPR spectra (c) of three samples and the photocatalytic activities (d) for the MPS selective conversion of different samples.

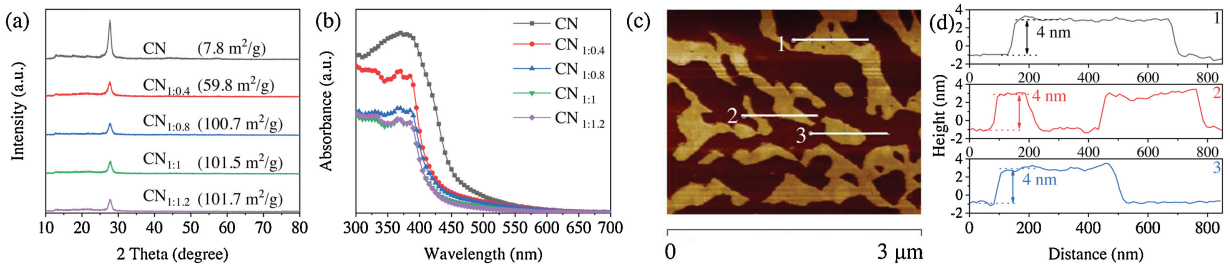

Fig. 3. XRD patterns (a) and UV–vis spectra (b) of different CN samples. AFM image (c) and corresponding height profiles (d) of $CN_{1:1}$ nanosheets.

patterns of ultrathin $CN_{1:X}$ nanosheets appear the weaker diffraction peaks, suggesting that the thicknesses of ultrathin $CN_{1:X}$ nanosheets are decreased [39]. Meanwhile, it is can be seen from the BET test that the specific surface areas of ultrathin $CN_{1:X}$ nanosheets increase with increasing the amount of cyanic acid, and finally get saturated at the ratio of 1:1, where the thinnest $CN_{1:X}$ nanosheet is obtained. In addition, the gradually decreased thicknesses of ultrathin $CN_{1:X}$ nanosheets are also reflected by the in-turn blue-shifted UV–vis band-edge absorption spectra in Fig. 3b [39,40]. As shown in Fig. 3c and Fig. S3 (Supporting information), the thicknesses of ultrathin $CN_{1:X}$ nanosheets and CN are characterized by the AFM test. The ultrathin $CN_{1:1}$ nanosheet exhibits the uniform few-layered structures with micro lateral dimension and an average thickness of ~4 nm for the ultrathin $CN_{1:1}$ nanosheet is evaluated from the height profiles in Fig. 3d.

The regulation effects of resulting $CN_{1:X}$ nanosheets layered structures on triplet excitons and then subsequent $^1O_2$ generation were further evaluated for optimizing the photoactivity for MPS oxidation. As shown in Fig. 4a, the PH intensity of ultrathin $CN_{1:X}$ nanosheet increases with the gradually decreasing thicknesses and then get the maximum on the ultrathin $CN_{1:1}$ nanosheet, indicating the highest density of triplet excitons in the ultrathin $CN_{1:1}$ nanosheet. Besides, the absolute PH quenching spectra of the ultrathin $CN_{1:X}$ nanosheets are recorded by the evaluated difference between the steady-state PH spectra in N_2 and in $^3O_2$. As shown in Fig. 4b, the absolute PH quenching intensities of the ultrathin $CN_{1:X}$ nanosheets become large simultaneously with the in-turn decreased thickness, suggesting that it is much favorable for the triplet excitons to be quenched by $^3O_2$ molecules to generate more $^1O_2$ because of the high specific surface areas on the thinner $CN_{1:X}$ nanosheets. According to the EPR spectra as shown in Fig. 4c, it is confirmed that the gradually strengthened 1:1:1 triplet signals of $^1O_2$ with the g value of 2.005 arise, and the EPR signal of optimal $CN_{1:1}$ nanosheet is about 4-time higher than that of pristine CN, indicating the increasing $^1O_2$ generation which results in the high conversion rate and selectivity. As expected, the photocatalytic oxidation rates of MPS are proportional to the amount of $^1O_2$ (Fig. S4 in Supporting information), and one can notice from the Fig. 4d that the conversion rate rises from ~16% for pristine CN to ~99% for the optimal $CN_{1:1}$ nanosheet with 5-time improvement after photocatalytic reaction for 3 h. Moreover, the optimal $CN_{1:1}$ nanosheet exhibits the maximum selectivity of ~99%. This clearly demonstrates that the optimal $CN_{1:1}$ nanosheet photocatalysts could be used to effectively convert MPS to desirable methyl phenyl sulfoxide with high selectivity due to the feature of generated $^1O_2$ *via* excitonic energy transfer processes.

As shown in Scheme S1 (Supporting information), a schematic diagram is proposed for efficient $^1O_2$ generations *via* excitonic energy transfer on ultrathin CN nanosheets. The irradiation with a bright lamp excites the ultrathin CN nanosheets to generate singlet state excitons, which then undergoes ISC to the longer-lived triplet state (T_1). The triplet state excitons transfer its energy to the $^3O_2$ molecules for $^1O_2$ generation and then return to the ground state (S_0). After that, $^1O_2$ molecules act as an effective oxidant for selective conversion of MPS molecules to methyl phenyl sulfoxide molecules in the sulfoxidation reaction through the formation of persulfoxide intermediate [6]. Therefore, the selective photocatalytic oxidation of MPS is close related to the excitonic energy transfer processes for $^1O_2$ formation.

In summary, we have systematically compared the excitonic aspects involved in pristine CN and BiOBr, and general P25 TiO_2 by combining SPC test, PH spectroscopy and EPR spectroscopy. Strong exciton effect caused by large intrinsic exciton binding energy on photocatalysts is responsible for the high selective photocatalytic oxidation of MPS. It is demonstrated that the 2D confined layered structures could intrinsically enhance the exciton effect in photocatalysts, and thus these photocatalysts generally possess more triplet excitons for $^1O_2$ generations. In addition, it is confirmed that the thinner CN nanosheets exhibit higher densities of the triplet excitons and more $^1O_2$ generations, which increase the conversion rate up to ~99% and the selectivity up to ~99% on the optimized ultrathin CN nanosheet (~4 nm). This work not only develops a feasible strategy to regulate the amount of $^1O_2$ molecules generated by the excitonic energy transfer for CN-based photocatalysts, but also establishes a novel mechanistic understanding on the excitonic processes.

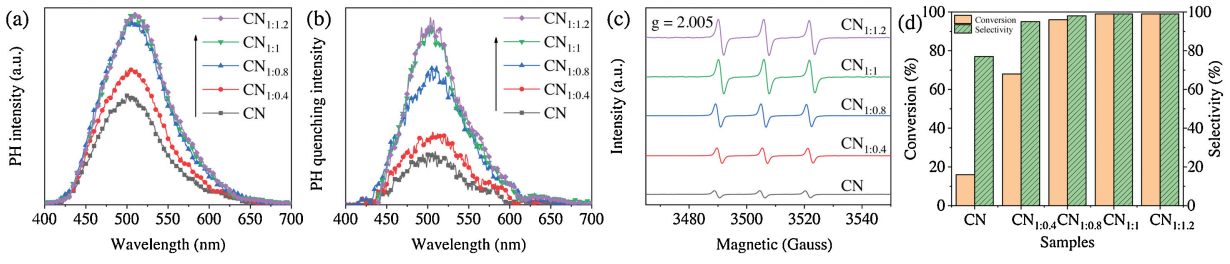

Fig. 4. PH spectra (a), absolute PH quenching spectra (b), EPR spectra (c) and the photocatalytic activities and selectivities of different CN samples.

Declaration of competing interest

The authors declare that they have no known competing financial interests or personal relationships that could have appeared to influence the work reported in this paper.

Acknowledgments

We are grateful to financial support from NSFC (Nos. U1805255, 11804086, 21706044, 21971057), General Financial Grant from the China Postdoctoral Science Foundation (No. 2017M621316), the Natural Science Foundation of Heilongjiang Province, China (No. B2017006) and the General Financial Grant from the Postdoctoral Science Foundation of Heilongjiang Province, China (No. LBH-Z17187) and the General Financial Grant from Heilongjiang Province for returned students from overseas in 2018.

Appendix A. Supplementary data

Supplementary material related to this article can be found, in the online version, at doi:https://doi.org/10.1016/j.cclet.2020.07.033.

References

[1] C. Dai, J. Zhang, C. Huang, Z. Lei, Chem. Rev. 117 (2017) 6929–6983.
[2] L. Chen, J. Tang, L.N. Song, et al., Appl. Catal. B: Environ. 242 (2019) 379–388.
[3] T.K. Kapuge, W.R.K. Thalgaspitiya, D. Rathnayake, et al., Appl. Catal. B: Environ. 268 (2020) 118386.
[4] C. Leal Marchena, G. Pecchi, L. Pierella, Mol. Catal. 482 (2020) 110685.
[5] P. Chen, Z. Guo, X. Liu, et al., J. Mater. Chem. A 7 (2019) 27074–27080.
[6] H. Wang, S. Jiang, S. Chen, et al., Adv. Mater. 28 (2016) 6940–6945.
[7] H. Wang, S. Jiang, S. Chen, et al., Chem. Sci. 8 (2017) 4087–4092.
[8] W. Wu, C. Han, Q. Zhang, et al., J. Catal. 361 (2018) 222–229.
[9] A. Zada, M. Humayun, F. Raziq, et al., Adv. Energy Mater. 6 (2016) 1601190.
[10] K. Matsubara, M. Inoue, H. Hagiwara, T. Abe, Appl. Catal. B: Environ. 254 (2019) 7–14.
[11] K. Bhattacharyya, J. Majeed, K.K. Dey, et al., J. Phys. Chem. C 118 (2014) 15946–15962.
[12] Z. Yu, H. Liu, M. Zhu, Y. Li, W. Li, Small 15 (2019) 1903378.
[13] J.L. Shi, X. Lang, Chem. Eng. J. 392 (2020) 123632.
[14] H. Wang, S. Chen, D. Yong, et al., J. Am. Chem. Soc. 139 (2017) 4737–4742.
[15] W. Jiang, H. Wang, X. Zhang, Y. Zhu, Y. Xie, Sci. China Chem. 61 (2018) 1205–1213.
[16] Z. Zeng, Y. Fan, X. Quan, et al., Water Res. 177 (2020) 115798.
[17] S. Melissen, T. Le Bahers, S.N. Steinmann, P. Sautet, J. Phys. Chem. C 119 (2015) 25188–25196.
[18] Y. Chen, H. Zhang, R. Lu, A. Yu, Chin. Chem. Lett. 29 (2018) 543–546.
[19] G. Zhang, A. Chaves, S. Huang, et al., Sci. Adv. 4 (2018) 1–7.
[20] Y. Peng, C. Xia, Z. Tan, J. An, Q. Zhang, Phys. Chem. Chem. Phys. 21 (2019) 26515–26524.
[21] P.C. Sercel, J.L. Lyons, N. Bernstein, A.L. Efros, J. Chem. Phys. 151 (2019) 234106.
[22] Y. Chen, D. Wang, Y. Lin, X. Zou, T. Xie, J. Power Sources 442 (2019) 227222.
[23] Q. Qiu, S. Li, J. Jiang, et al., J. Phys. Chem. C 121 (2017) 21560–21570.
[24] M.C. DeRosa, R.J. Crutchley, Coord. Chem. Rev. 233 (2002) 351–371.
[25] D. Kovalev, M. Fujii, Adv. Mater. 17 (2005) 2531–2544.
[26] K. Zhang, D. Kopetzki, P.H. Seeberger, M. Antonietti, F. Vilela, Angew. Chem. Int. Ed. 52 (2013) 1432–1436.
[27] P. Liang, C. Zhang, X. Duan, et al., ACS Sustain. Chem. Eng. 5 (2017) 2693–2701.
[28] Z. MacHatova, Z. Barbieriková, P. Poliak, et al., Dyes Pigm. 132 (2016) 79–93.
[29] Y.S. Jun, E.Z. Lee, X. Wang, et al., Adv. Funct. Mater. 23 (2013) 3661–3667.
[30] A.H. Proppe, M.H. Elkins, O. Voznyy, et al., J. Phys. Chem. Lett. 10 (2019) 419–426.
[31] D. Kim, M. Lee, S.Y. Song, et al., J. Phys. Chem. C 120 (2016) 18674–18681.
[32] E. Berardo, M.A. Zwijnenburg, J. Phys. Chem. C 119 (2015) 13384–13393.
[33] C. Zheng, S. Yu, O. Rubel, Phys. Rev. Mater. 2 (2018) 1–11.
[34] Y. Xing, L. Wang, C. Liu, X. Jin, Sensors Actuators B: Chem. 304 (2020) 127378.
[35] N. Notsuka, H. Nakanotani, H. Noda, K. Goushi, C. Adachi, J. Phys. Chem. Lett. 11 (2020) 562–566.
[36] Q. Chen, L. Chen, J. Qi, et al., Chin. Chem. Lett. 30 (2019) 1214–1218.
[37] H. Liang, P. Hua, Y. Zhou, et al., Chin. Chem. Lett. 30 (2019) 2245–2248.
[38] A.D. Tjandra, J. Huang, Chin. Chem. Lett. 29 (2018) 734–746.
[39] J. Yan, C. Zhou, P. Li, et al., Colloids Surfaces A Physicochem. Eng. Asp. 508 (2016) 257–264.
[40] H. Lv, Y. Huang, R.T. Koodali, et al., ACS Appl. Mater. Interfaces 12 (2020) 12656–12667.